

Cryogenic interface-state filling and tunneling mechanisms in strained Ge/SiGe heterostructures

Jingrui Ma^{1,2,§}, Yuan Kang^{1,2,3,§}, Rui Wu^{1,2}, Zheng Liu^{1,2}, Zong-Hu Li^{1,2}, Tian-Yue Hao^{1,2}, Zhen-Zhen Kong^{3,4}, Gui-Lei Wang^{3,4,†}, Yong-Qiang Xu^{1,2}, Ran-Ran Cai^{1,2}, Bao-Chuan Wang^{1,2,3}, Hai-Ou Li^{1,2,3}, Gang Cao^{1,2,3,*}, and Guo-Ping Guo^{1,2,3,5}

¹*Laboratory of Quantum Information, University of Science and Technology of China, Hefei, Anhui 230026, China*

²*CAS Center for Excellence in Quantum Information and Quantum Physics, University of Science and Technology of China, Hefei, Anhui 230026, China*

³*Hefei National Laboratory, Hefei, Anhui 230088, China*

⁴*Beijing Superstring Academy of Memory Technology, Beijing 100176, China*

⁵*Origin Quantum Computing Company Limited, Hefei, Anhui 230088, China*

* Contact author: gcao@ustc.edu.cn

† Contact author: guilei.wang@bjsamt.org.cn

§ The authors have equally contributed in this article.

ABSTRACT. Traps at the semiconductor-oxide interface are considered as a major source of instability in strained Ge/SiGe quantum devices, yet the quantified study of their cryogenic behavior remains limited. In this work, we investigate interface-state trapping using Hall-bar field-effect transistors fabricated on strained Ge/SiGe heterostructures. Combining transport measurements with long-term stabilization and Schrödinger-Poisson modelling, we reconstruct the gradual filling process of interface states at cryogenic condition. Using the calculated valence band profiles, we further evaluate the tunneling current density between the quantum well and the semiconductor-oxide interface. Our calculation demonstrates that the total tunneling current is consistent with a crossover from trap-assisted-tunneling-dominated transport to Fowler-Nordheim-tunneling-dominated transport under different gate bias regimes. These results refine the conventional Fowler-Nordheim-based picture of interface trapping in strained Ge/SiGe heterostructures and provide guidelines for improving Ge-based quantum device performance by improving barrier crystalline qualities and reducing dislocation-related trap densities.

I. INTRODUCTION.

Semiconductor spin qubits have emerged as a platform for scalable quantum computing. Among the available material platforms, germanium has attracted significant attention, owing to its strong spin-orbit coupling, weak hyperfine effect and strain-induced splitting between heavy- and light-hole states [1–6]. In recent years, impressive progress has been achieved with germanium hole qubits, such as two-dimensional qubit arrays [7–10], high-fidelity quantum gate [4,11,12], coupling with microwave resonators [13–16] and spin shuttling [8,17]. These advances highlight strained Ge as a promising material for future quantum technologies. However, the practical performance of germanium-based quantum device is strongly limited by interface traps. These traps arise from a high density of dangling bonds at semiconductor-oxide interface due to incomplete oxidation under ambient conditions [18–20] and can capture carriers. Specifically, when a negative gate voltage is applied to a germanium quantum device, the two-dimensional hole gas (2DHG) is accumulated in the Ge quantum well (QW), forming a conduction channel. In this process, free holes in the 2DHG may tunnel through the SiGe barrier and reach the semiconductor-oxide interface, where they are captured by traps and form positive fixed charges [21–23]. The presence of these positive charges partially shields the gate voltage, reducing the effective electric field applied to the quantum well. As a result, the channel's conductivity is weakened and the device drifts away from its intended operating point. In order to compensate this effect, a more negative voltage is then required. However, as long as the interface traps are not fully filled, further trapping and threshold voltage drift will occur, causing long-term instability [6,21–29] and complicating measurements and operation in Ge-based devices.

Despite the critical impact on device stability, interface traps in germanium heterostructures have only been studied in a few specific contexts. Previous studies have qualitatively demonstrated the presence of interface states and their influence on device operation [21,22,30,31], and several works have

focused on reducing interface state density by chemical treatments and passivation techniques [20,23,27,32]. However, a deeper understanding of interface-state behavior at cryogenic temperatures remains limited.

In this work, we address this challenge by combining cryogenic transport measurements on strained Ge (sGe) heterostructures with numerical simulations to investigate the behavior and mechanism of interface states. By analyzing the gate-voltage dependence of trapped charge from an inverted Schrödinger-Poisson model, we infer the density of occupied interface states as a function of gate voltage and provide quantitative estimates of traps at low temperature. In addition, we also investigate the microscopic mechanism that supports interface trapping by evaluating tunneling current density within the Ge/SiGe heterostructure. While previous works interpret trapping process in terms of Fowler-Nordheim (F-N) tunneling [21–23], our analysis additionally suggests possible contribution from trap-assisted tunneling (TAT) under certain conditions. This approach that combines experimental and inverse numerical modeling enables us to extract the properties of interface states under cryogenic conditions. Our results not only provide insight into the cryogenic mechanisms governing trap dynamics in strained Ge, but also suggest promising optimization directions in future quantum devices.

II. EXPERIMENT SETUP

The device under test is fabricated on a reverse-graded strained germanium heterostructure whose profile is illustrated in Fig. 1(a). The Ge/SiGe heterostructure consists of a strained germanium quantum well with thickness of 16 nm and a 32 nm $\text{Si}_{0.2}\text{Ge}_{0.8}$ barrier layer. This configuration of

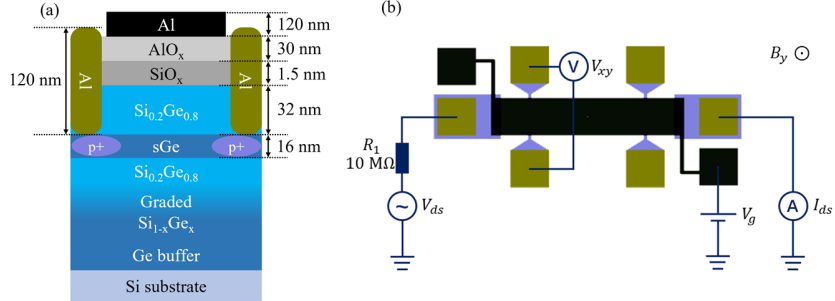


FIG. 1. (a) Cross-sectional view of Hall-bar FET gate stack as well as sGe quantum well configuration. (b) Schematic of FET device and measurement circuit. A resistor R_1 is introduced to prevent current overload within the circuit.

germanium quantum well is similar to that used in Refs. [5] and [23].

In order to observe various phenomena caused by interface defects, the Hall-bar-type field-effect transistor (Hall-bar FET) is fabricated on top of this material stack. As shown in Fig. 1(a) and (b), the enhancement p-type Hall-bar FET consists of a metallic top gate (black), gate oxide (grey), source-drain electrodes (brown) and p-doped contact regions (light purple). When a negative voltage V_g is applied to the top gate, the undoped sGe/SiGe quantum well experiences an electric field across the gate oxide and an accumulation channel will be formed in the QW.

During measurement, the device is mounted in a refrigerator and cooled down to ≈ 4.5 K. The measurement setup is schematically shown in Fig. 1(b). A DC voltage source is connected to the aluminum top gate to provide gate bias V_g . A small AC source-drain excitation V_{ds} is applied using a lock-in amplifier and the resulting current I_{ds} is measured. Meanwhile, an out-of-plane magnetic field B_y is provided by the vector magnet, under which a transverse Hall voltage V_{xy} will be induced perpendicular to the direction of I_{ds} and detected by a second lock-in amplifier.

III. RESULTS

A. Quasistatic hole density measurements

The experiments on source-drain current and hole density are conducted cyclically while sweeping the voltage on top gate, following the protocol illustrated in Fig. 2(a). Each individual cycle is defined by a chosen value of V_{min} . At the beginning of each cycle, we firstly set $V_g = 0$ to initialize the measurement. After initialization, V_g is set to V_{min} to turn on the FET. Once 2DHG is formed in the channel, we hold

$V_g = V_{min}$ for a duration $T_{meas} \approx 24000$ s, during which I_{ds} is continuously recorded, yielding the trace of time-dependent source-drain current $I_{ds}(t)$. After this waiting period, we sweep B_y and measure transverse voltage V_{xy} . By fitting linearly into $\rho_{xy} = B_y/ep_{2DHG} + c$, where e is the elementary charge, $\rho_{xy} = V_{xy}/I_{ds}$ is Hall resistivity and c is a small offset, we extract the hole density p_{2DHG} under this specific V_g . This completes one cycle and the protocol is repeated with a more negative value of V_{min} .

The full set of $I_{ds}(t)$ under different V_{min} is shown in Fig. 2(b). All curves of current in the figure exhibit a decay before reaching a stabilized value. This behavior is attributed to the leakage within the heterostructure: holes in the 2DHG tunnel through the barrier and are subsequently captured by interface states, as also reported in previous works [23] on Ge-based FETs. We assume that after T_{meas} the system is quasistatic, and the measured p_{2DHG} at this point reflects the final trapped-charge configuration under the corresponding V_g . Figure 2(c) illustrates an example of $V_{xy}(B_y)$ traces after current stabilization. Using the relationship of $V_{xy}(B_y)$, we extract carrier density under each V_{min} as summarized in Fig. 2(d). These stabilized values of p_{2DHG} are of more interest in this work since they form the key experimental input for numerical modelling, which is demonstrated in the next section.

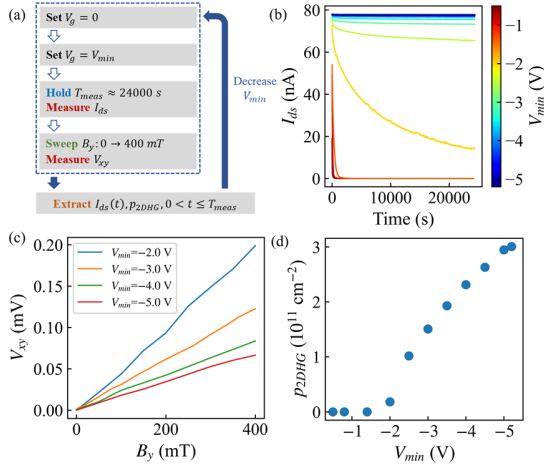


FIG. 2. Quasistatic hole density measurements and results. (a) Measurement protocol of the whole process. (b) Extracted curve of long-term stability of source-drain current $I_{ds}(t)$ under different V_{min} . (c) Example of Hall voltage while sweeping the out-of-plane magnetic field. The relationship of $V_{xy}(B_y)$ is then used to compute carrier density in (d). (d) Extracted 2DHG sheet density p_{2DHG} under different V_{min} , each point in the figure is extracted after I_{ds} is stabilized, *i.e.*, after the rightmost point of each curve in (b).

B. Schrödinger-Poisson Modelling and Extraction of Interface Charge

In order to infer the amount of filled interface states from experimental data at each gate voltage, we build an one-dimensional self-consistent Schrödinger-Poisson (S-P) solver [33,34]. The S-P solver takes gate voltage V_g and interface charge density p_{it} as input parameters and returns valence band profile $E_v(x)$ as well as corresponding theoretically calculated carrier density $p_{2DHG,th}$ (see Appendix A for more details). An example of S-P calculation result is shown in Fig. 3(a) for $V_g = -0.5$ V and $p_{it} = 0$. As the valence band edge in Ge QW bends upward and rises above the Fermi level, 2DHG is formed and accumulated in the channel, which is reflected experimentally as a finite I_{ds} . In compact form, the S-P simulation can be written as a single mapping:

$$(E_v(x), p_{2DHG,th}) = F(V_g, p_{it}). \quad (1)$$

In our analysis, V_g is given as a boundary condition, the experimental 2DHG density $p_{2DHG,exp}$ is obtained from Hall measurements, and p_{it} is the unknown value to be solved. Thus, extracting p_{it} is equivalent

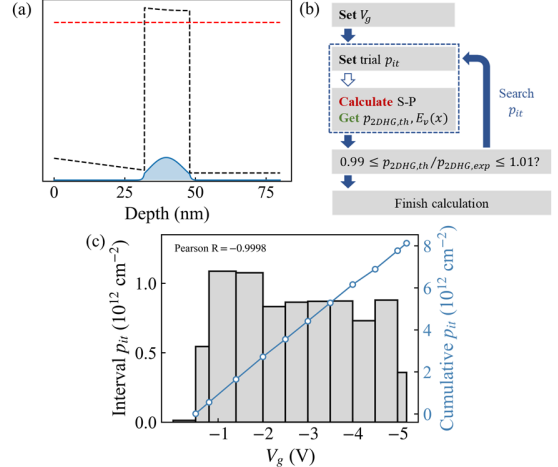


FIG. 3. (a) Example of self-consistent S-P calculation. The black dashed line shows the valence band profile along the 1D mesh, red horizontal line indicates Fermi level. Shaded area shows the simulated hole wavefunction. Note that this profile only shows the SiGe/sGe/SiGe region. (b) Calculation process of inferring p_{it} from V_g and $p_{2DHG,exp}$. (c) Accumulation of p_{it} vs V_g and the amount of interface charge in each gate voltage interval. Pearson R value is calculated using cumulative density and V_g .

to inverting Eq. (1), which we treat as a root-finding problem. For each fixed V_g , we scan different trial values of p_{it} , run the S-P solver to get corresponding $p_{2DHG,th}$, and compare it with $p_{2DHG,exp}$. In order to improve numerical stability, we accept the solution when the following condition is satisfied:

$$0.99 \leq p_{2DHG,th}/p_{2DHG,exp} \leq 1.01. \quad (2)$$

The p_{it} value that satisfies Eq. (2) is returned as the saturated interface charge under that V_g . A summary of this workflow is illustrated in Fig. 3(b). By repeating this procedure for each data point in Fig. 2(d), we would be able to reconstruct how the interface charge is built up with gate voltage. Figure 3(c) illustrates the resulting p_{it} as a function of V_g (blue line), together with the density of interface states being filled in each voltage interval (grey bars). As indicated by Pearson correlation coefficient in Fig. 3(c), we find that the inferred trapped charge increases almost linearly with $|V_g|$ over the explored range, consistent with a capacitor-like response of the semiconductor-oxide interface stack. This inverted S-P method effectively resolves intermediate values of trap filling under cryogenic conditions, which, to our knowledge, have not been quantified in existing studies.

C. Tunneling current density Calculation

The analysis in the previous section provided the equilibrium density of occupied interface states as a function of gate voltage. Based on these results, we intend to further study how holes in 2DHG reach interface traps, and investigate the microscopic tunneling process across the quantum well barrier. Specifically, we use the valence band profile obtained from S-P solver (Eq. (1)) as input to calculate the tunneling current density. Our goal is to estimate the tunneling current density from the QW to the semiconductor-oxide interface and identify the tunneling mechanism under the experimentally explored gate-voltage interval.

The tunneling current density is taken as the sum of three distinct tunneling mechanisms: direct tunneling, Fowler-Nordheim (F-N) tunneling and trap-assisted tunneling (TAT) [35], as illustrated in Fig. 4(a). The total current density is written as:

$$J_{\text{total}} = J_{\text{direct}} + J_{\text{FN}} = J_{\text{TAT}}. \quad (3)$$

Direct tunneling occurs when holes in Ge QW coherently tunnel through the entire SiGe barrier and reach the interface. For a rectangular barrier, the corresponding current density can be approximated as [36]:

$$J_{\text{direct}} \propto \exp\left(-\frac{2t\sqrt{2m^*}\phi_B}{\hbar}\right), \quad (4)$$

where ϕ_B is the barrier height, m^* is effective mass and t is the barrier thickness. When the band bending becomes strong (*i.e.*, under large negative gate bias), the barrier is reshaped approximately into a triangle and the tunneling is described by Fowler-Nordheim theory [37]. The F-N tunneling current density through a triangular barrier is given by [35–37]:

$$J_{\text{FN}} = \frac{e^3 E^2}{8\pi\hbar\phi_B} \exp\left(-\frac{8\pi\sqrt{2m^*}\phi_B^{3/2}}{3e\hbar E}\right), \quad (5)$$

Where E is the electric field across the barrier. In our calculation, both barrier height ϕ_B and electric field E are obtained from S-P simulation results.

Trap-assisted tunneling refers to a multi-step process in which holes reach the semiconductor-oxide interface via intermediate defect states in the barrier. Strain-induced misfit dislocations in the SiGe alloy may act as such intermediate sites and create tunneling pathways. Here, unless otherwise specified, the “trap” discussed in this section refers to defects within the barrier layer, instead of the interface states discussed previously. Existing studies report that typical dislocation densities in SiGe could reach the order of 10^6 to 10^8 cm $^{-2}$ [2,38–40], which we consider sufficient to provide a dense net of intermediate sites for hole tunneling. The TAT current density is

obtained by integrating the contribution over the whole layer since the process may occur at any position within the barrier. The analytical form of J_{TAT} is written as [35]:

$$J_{\text{TAT}} = e \int_0^L \frac{N_T(x)}{\tau(x)} dx, \quad (6)$$

where $N_T(x)$ is the distribution of trap, $\tau(x)$ is a parameter that combines the trap’s local capture and emission rate. Numerically, we implement the calculation of J_{TAT} by:

$$J_{\text{TAT}} = e \sum_{i=1}^m p_i \cdot \sigma \cdot \left(\sum_j \Delta x \cdot N_{T,j} \cdot TC_j \right), \quad (7)$$

Where p_i is the supply hole density from the i -th subband, σ is the hole capture cross section. The supply hole density at each subband is given by:

$$p_i = k_B T \frac{m^* m_e}{\pi \hbar^2} \ln \left[1 + \exp \left(\frac{E_i - E_F}{k_B T} \right) \right], \quad (8)$$

where E_i is the i -th eigenenergy computed from Schrödinger’s equation, E_F is the Fermi level, m_e is the electron mass and $T = 4.5$ K is the temperature of simulation. The last term in Eq. (7) is the integration’s numerical form. Δx is the mesh size, $N_{T,j}$ is the trap density at the j -th point and TC_j is the tunneling coefficient. The tunneling coefficient reflects the rate of hole tunneling between adjacent trap sites, and is evaluated under the Wentzel-Kramers-Brillouin (WKB) approximation [41–43]. The trap density $N_{T,j}$ is sampled from a distribution in both space and energy:

$$N_{T,j} = w(\mu_{\text{trap}}, \sigma_{\text{trap}}) N_T(x), \quad (9)$$

where w is the weight indicating trap distribution in energy. In this work, we assume that traps follow a Gaussian distribution in energy [35], characterized by a specified mean value μ_{trap} and standard deviation σ_{trap} . Meanwhile, $N_T(x)$ is the trap density calculated from a spatial distribution. Dislocation-related traps are considered to originate at the Ge/SiGe interface, so that the trap density is maximal at this interface and decrease as moving away from it. We use an exponential decay profile to phenomenologically describe this distribution along the growth direction:

$$N_T(x) = N_{\text{trap}} \exp\left(-\frac{x - x_0}{\lambda}\right), \quad (10)$$

where N_{trap} is the largest trap density at Ge/SiGe interface ($x = x_0$), and λ is a characteristic length of a few nanometers.

Using the equations above, the calculated tunneling current density for direct tunneling, F-N tunneling and TAT are shown in Fig. 4(b), (c), (e) respectively. The current density associated with direct tunneling is constantly negligible (approximately 10^{-30} A/m^2) over the entire gate-voltage range, which is expected since J_{direct} scales exponentially with thickness of the barrier according to Eq. (4). In our heterostructure, the $t = 32 \text{ nm}$ barrier (Fig. 1(b)) strongly suppresses direct tunneling, which was also suggested by existing works [21,22]. In contrast, the F-N current density experiences a strong turning point at $V_g \approx -4.0 \text{ V}$.

This behavior reflects J_{FN} 's strong dependence on electric field, which is directly linked to the valence-band profile. As shown in the insets of Fig. 4(c), the Ge/SiGe valance band evolves from weak to strong bending as more negative V_g is applied. The specific value of this turning point is mainly determined by the thickness of the SiGe barrier, as illustrated in Fig. 4(d). Notably, Figure 4(d) is simulated without considering interface traps, hence the simulation range of voltage differs from that in other figures. For a thicker barrier, holes more difficult to tunnel through, and stronger gate voltage is required to achieve the same tunneling current.

Meanwhile, TAT current density, shown in Fig. 4(e), remains mostly within the same order of magnitude within the explored range of V_g . Here, we observe a slight decrease of J_{TAT} at the most negative gate voltages. In our model, this behavior reflects the fact that TAT is primarily governed by trap properties [35]. While the WKB tunneling coefficient TC increases with $|V_g|$ as the electric field is enhanced, this term does not outperform the change in trap distribution N_T . Dislocation-related traps in SiGe have been reported at energies above the valence-band edge at approximately 140 meV [44,45], whereas the valence-band offset between sGe QW and SiGe barrier in our heterostructure is only $\sim 114 \text{ meV}$ [22,46]. As the gate bias becomes more negative, the stronger band bending makes subband energies move further away from μ_{trap} , hence reducing the Gaussian weight w associated with the total trap density (Eq. (9)) and compensating the increase in tunneling coefficient. We emphasize that this decrease in J_{TAT} does not affect the following analysis of tunneling current contribution. It should also be noted though, since many microscopic trap parameters are not directly

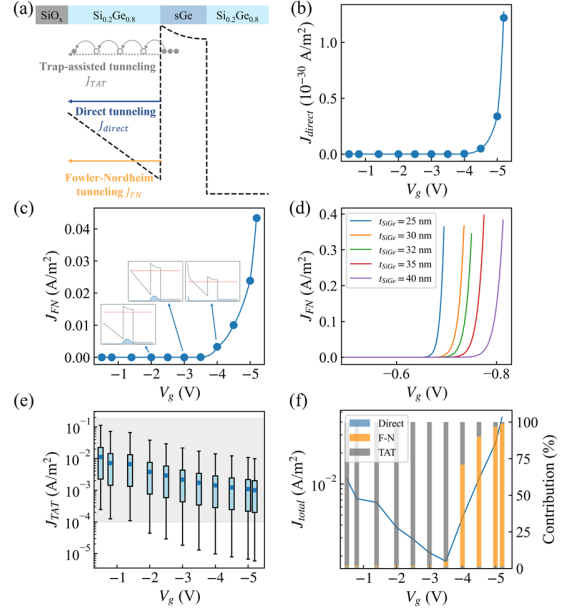


FIG. 4. (a) Illustration of direct tunneling, Fowler-Nordheim tunneling and trap-assisted tunneling within the Ge/SiGe heterostructure. (b) Direct and (c) F-N tunneling current density as a function of V_g . Insets: Valence band simulation at $V_g = -2, -3, -4 \text{ V}$ respectively. (d) Comparison of J_{FN} simulated under different SiGe barrier thickness. Note that this calculation is performed assuming $p_u = 0$. (e) TAT current density as a function of V_g . Blue scatters indicate J_{TAT} under default parameter, boxes indicate J_{TAT} under varied trap parameters in TABLE I, grey shaded area indicates J_{TAT} order consistent with experiments. (f) Total current density (blue line) as well as the contribution percentage of each mechanism. Blue bar indicates direct tunneling ($\ll 1\%$), orange bar indicates F-N tunneling and grey bar indicates TAT contribution.

accessible in our experiment, the J_{TAT} calculation is intended to provide an order-of-magnitude estimate, rather than to obtain a fairly precise value of J_{TAT} . We used dislocation-related trap parameters reported in literatures, as summarized in TABLE I, to perform a parameter sweep and support our TAT estimation (see Appendix B for more details). The grey shaded area in Fig. 4(e) indicates the reasonable range of J_{TAT} corresponding to our device. For our Hall-bar FET with gate area of $S \approx 1 \times 10^{-7} \text{ m}^2$, the current density in the shaded area provides tunneling current between 10 pA to tens of nA, which is consistent with measured channel current in Fig. 2(b). We observe that under

TABLE I. Key parameter range used in TAT current density calculation in strained Ge/SiGe heterostructure.

Parameter	Baseline value	Test range	Unit	Refs.
N_{trap}	1×10^7	$[1 \times 10^6, 1 \times 10^8]$	cm^{-2}	[2,39,40,47]
σ	8×10^{-17}	$[5 \times 10^{-18}, 2 \times 10^{-16}]$	cm^2	[45,48]
μ_{trap}	$E_v + 140$	$[E_v + 120, E_v + 160]$	meV	[44,45]

physically sound trap parameters, the results of J_{TAT} mostly fall into this range, hence providing a possible leakage path with the correct order of magnitude to account for the interface-state filling under small $|V_g|$ observed in the experiment.

The total tunneling current density, along with the relative contribution of each mechanism, is then plotted in Fig. 4(f). The direct-tunneling contribution remains well below 1% for all gate voltages. It is therefore clear that the tunneling process in strained Ge is effectively a two-mechanism problem, dominated separately by TAT and F-N tunneling in different gate voltages. At small $|V_g|$, the electric field within the heterostructure is insufficient to support significant F-N tunneling, and holes in 2DHG most likely travel through dislocation-induced traps in SiGe barrier towards the surface. In this case, we suggest that the total tunneling current is dominated by TAT under physically reasonable parameters, after which holes are captured by interface states. As the gate bias becomes more negative, although the contribution of TAT still exists, its weight becomes smaller compared to the rapidly increasing F-N tunneling current density supported by electric field. Therefore, under the $V_g \leq -4.0$ V regime, a description based on F-N is a good approximation of the tunneling-trapping process. Comparing to previous studies that qualitatively interpreted interface trapping in terms of F-N tunneling alone [21–23], our calculations indicate that for realistic barrier parameters, an F-N-only model underestimates the current at small and moderate fields. This extends the conventional F-N-based picture by demonstrating that TAT supported by dislocation-related defects provides a natural explanation for the observed interface accumulation at small negative voltages.

IV. DISCUSSION

To further support our tunneling analysis and test whether the prominence of TAT at small and moderate fields is an artifact of uncertain trap parameters, we perform the same analysis to a representative strained-Si/SiGe quantum well. As shown in Fig. 5(a), the reference structure contains a 15 nm undoped Si layer

buried 25 nm deep into the $\text{Si}_{0.7}\text{Ge}_{0.3}$ barrier, with a conduction band offset of approximately 180 meV [46,49,50]. Following the procedure described in Sec. III C, we first use the S-P solver to obtain the self-consistent conduction band profile (Fig. 5(b)), then compute the corresponding J_{FN} and J_{TAT} in silicon using literature-based defect parameters summarized in TABLE II.

The comparisons of J_{FN} and J_{TAT} between Si/SiGe and Ge/SiGe heterostructures are illustrated in Fig. 5(c) and Fig. 5(d) respectively. Since Si- and Ge-based devices have different working regime, we choose to use electric field, rather than gate voltage, to better visualize data. We find that F-N tunneling current densities are of similar magnitude for both stacks, consistent with the fact that J_{FN} is controlled by the electric field. Differences in the specific onset of J_{FN} mainly reflect influence of other barrier parameters (barrier height, effective mass and thickness) and is beyond the scope of this work. By contrast, the calculated J_{TAT} in strained Si is suppressed by roughly one to three orders of magnitude compared to the Ge case under moderate field range. This could be explained naturally by the difference in trap parameters between TABLE I and TABLE II. In particular, the dislocation-related trap density assumed for Si/SiGe is lower, and the trap energy distribution is located far deeper relative to the tunneling window, hence reducing the effective contribution of traps in calculation. Although the effective electron capture cross section in Si is significantly larger than the corresponding hole capture cross section in Ge, this does not outperform the other two factors, yielding a total suppression of J_{TAT} in the Si/SiGe heterostructure.

These comparative results support a physical picture where defect-mediated pathways could enable significant tunneling at small and moderate fields in strained Ge/SiGe, whereas the high-electric-field regime is governed predominantly by F-N tunneling in both material systems. Experimentally, the pronounced current decay observed in our Ge/SiGe devices (Fig. 2(b)) is consistent with this two-regime picture, while related studies on Si/SiGe report slower evolution of channel resistivity [51] in the absence of

TABLE II. Key parameter range used in TAT current density calculation in strained Si/SiGe heterostructure.

Parameter	Baseline value	Test range	Unit	Refs.
N_{trap}	1×10^6	$[1 \times 10^5, 1 \times 10^7]$	cm^{-2}	[52–55]
σ	4×10^{-12}	$[1 \times 10^{-13}, 1 \times 10^{-12}]$	cm^2	[56]
μ_{trap}	$E_c - 600$	$[E_c - 620, E_c - 580]$	meV	[56]

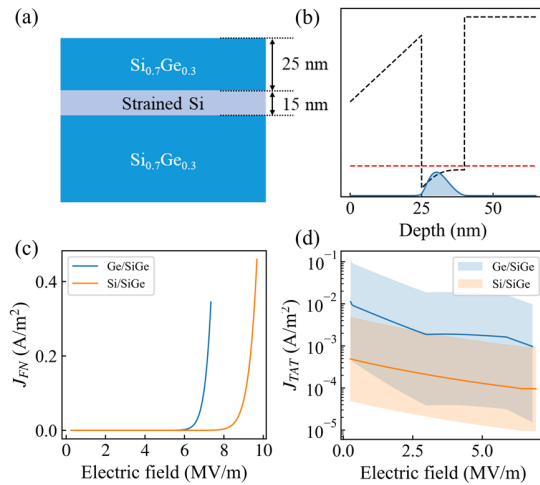


FIG. 5. (a) Representative material stack used in calculation. Note that no interface states are considered. (b) Example of conduction band profile and electron wavefunction from S-P solver. (c) Comparison of J_{FN} and (d) J_{TAT} between Ge/SiGe and Si/SiGe heterostructures. Shaded areas in (d) indicate J_{TAT} estimated under varied trap properties in TABLE I, II for Ge and Si QW respectively.

enough defect-mediated tunneling pathways from our calculation.

In addition to supporting the tunneling interpretation, our analysis highlights practical directions for heterostructure optimization. Increasing the barrier thickness can suppress F-N tunneling, as shown in Fig. 4(d). However, under small and moderate field regimes, which are most relevant to qubit operation, suppressing TAT pathways by defects in the SiGe barrier is expected to be particularly important. Improving crystalline quality during heterostructure growth to reduce dislocation-related trap densities should therefore strongly mitigate TAT and enhance device stability. This perspective is highly consistent with recent reports on lattice-matched Ge/SiGe heterostructures grown below the critical thickness [57–59], where significant improvements in material property and qubit performance have been reported [60–63]. Besides lattice matching, several complementary strategies

have also been demonstrated. On the materials side, optimized buffer designs and growth protocols can reduce threading-dislocation density in Ge-rich quantum wells [40,64]. On the device side, introducing a backgate provides an additional degree of freedom to tune the location of hole wavefunction [28], potentially reducing its overlap with defect-rich regions. Finally, surface passivation that reduce the semiconductor-oxide interface trap density [23,27,65–68] directly mitigate charge trapping near the surface. Taken together, these engineering approaches provide a practical pathway improving stability and scalability of germanium-based quantum devices.

V. CONCLUSIONS

In conclusion, we fabricated Hall-bar field-effect-transistors on strained Ge/SiGe heterostructures and investigated the mechanism behind interface-state trapping. Transport measurements after long-term stabilization at cryogenic temperatures as a function of gate bias allow us to extract quasistatic carrier density after the stabilization of transient current. Using these densities as constraints in an inverted Schrödinger-Poisson model, we reconstruct the sheet density of occupied interface states as a function of gate voltage, thereby quantifying the progressive filling of interface traps at low temperature. We then apply the simulated band profiles in tunneling models to evaluate the current density associated with direct, Fowler-Nordheim and trap-assisted tunneling. The combined experimental and modelling results support a two-regime transition from TAT-dominated at small and moderate fields to F-N-dominated tunneling at high fields, which extends the conventional interpretation that attributes interface trapping in strained Ge solely to F-N tunneling.

Beyond establishing this mechanism, our calculation provides practical guidance for device optimization. While increasing barrier thickness suppresses high-field leakage by F-N tunneling, mitigating tunneling pathways from dislocation-related defects is of importance. This highlights the necessity to improve crystalline quality and reduce dislocation trap densities as key routes to enhance future Ge-based quantum devices.

ACKNOWLEDGMENTS

This work was supported by the National Natural Science Foundation of China (12574552, 12474490, and 12304560), and Quantum Science and Technology-National Science and Technology Major Project (Grant No. 2021ZD0302300). This work was partially carried out at the University of Science and Technology of China Center for Micro and Nanoscale Research and Fabrication.

DATA AVAILABILITY

The data that support the findings of this article are not publicly available. The data are available from the authors upon reasonable request.

APPENDIX A: SELF-CONSISTENT SCHRÖDINGER-POISSON CALCULATION

In this section, we describe the details of numerical calculation. The self-consistent Schrödinger-Poisson (S-P) solver involves Schrödinger and Poisson equation coupled in two directions [33]. The 1D Schrödinger equation used in this model is time-independent and described by:

$$-\frac{\hbar^2}{2} \frac{d}{dx} \left(\frac{1}{m^*(x)} \frac{d}{dx} \right) \psi(x) + V(x) \psi(x) = E \psi(x), \quad (A1)$$

where ψ is the wavefunction, V is the potential, E is the eigenenergy and m^* is the effective mass. Solving Eq. (A1) yields a finite number of wavefunctions with corresponding eigenenergies. Meanwhile, the one-dimensional Poisson equation reads:

$$\frac{d}{dx} \left(\epsilon_r(x) \frac{d}{dx} \right) \phi(x) = -\frac{e}{\epsilon_0} p(x), \quad (A2)$$

where ϵ_r is the relative permittivity, ϕ is the electrostatic potential and p is the distribution of holes. On one hand, the resulting ϕ in Poisson equation is translated into V in Schrödinger equation by:

$$V(x) = -e\phi(x) + \Delta E_v(x), \quad (A3)$$

where ΔE_v is the valence band offset between germanium and $\text{Si}_{0.2}\text{Ge}_{0.8}$ in the QW. On the other hand, the hole wavefunction from Schrödinger is translated into hole density by:

$$p(x) = \sum_{i=1}^m \psi_i^*(x) \psi_i(x) p_i(x), \quad (A4)$$

where m is the total number of bound states and p_i is the occupation of holes within each state (subband). The concentration of holes for a certain state is represented by

$$p_i(x) = \frac{m^*(x)}{\pi \hbar^2} \int_{-\infty}^{E_i} \frac{1}{1 + e^{(E_F - E)/k_B T}} dE, \quad (A5)$$

where E_F is the Fermi level and E_i is the i -th eigenenergy solved from Eq. (A1).

In order to solve the equations above numerically, we firstly discretize Eq. (A1) along the one-dimensional finite-difference mesh:

$$-\frac{\hbar^2}{2} \frac{1}{\Delta x} \left(\frac{\psi_{i+1} - \psi_i}{m_{i+1/2}^* \Delta x} - \frac{\psi_i - \psi_{i-1}}{m_{i-1/2}^* \Delta x} \right) + V_i \psi_i = \lambda \psi_i, \quad (A6)$$

where i is the index of mesh point, Δx is the mesh size of the grid, and m^* with a half-integer index is the mid-point value constructed from effective mass in adjacent points. This reduces a differential equation to an eigenvalue problem of a tridiagonal matrix. Numerically solving Eq. (A6) yields a finite number of wavefunctions with corresponding eigenenergies.

As another part of the iteration, we solve Poisson's equation using Newton's method. Assume in the k -th iteration, we have a guess of electrostatic potential $\phi^{(k)}$, and inside the 1D Poisson equation, we have:

$$\frac{d}{dx} \left(\epsilon_r(x) \frac{d}{dx} \right) \phi^{(k)}(x) = -\frac{e}{\epsilon_0} p[\phi^{(k)}](x). \quad (A7)$$

Here, we write in $p[\phi^{(k)}](x)$ to explicitly indicate that the charge density depends on the electrostatic potential profile. This is because the hole density is derived from subbands in Schrödinger's equation, which are again determined by the electrostatic potential from the previous iteration of Poisson (Eqs. (A2), (A4) and (A5)). The left-hand side of Eq. (A7) is simply Laplacian of $\phi^{(k)}(x)$, with additional weights taken from dielectric constants. The right-hand side indicates the charge density calculated from this $\phi^{(k)}$, in other words, the value that the Laplacian should ideally equal to. Eq. (A7) holds only when the iteration is converged and the Poisson potential does not change with further calculations. By taking the difference of two sides, we define the residual function of Poisson equation at iteration k :

$$R^{(k)}(x) = \frac{d}{dx} \left(\epsilon_r(x) \frac{d}{dx} \right) \phi^{(k)}(x) + \frac{e}{\epsilon_0} p[\phi^{(k)}](x). \quad (A8)$$

This equation tells how far we are from satisfying Poisson equation for the current ϕ . If $R^{(k)} = 0$ everywhere, the self-consistency is then achieved. Using this residual, we would be able to calculate the correction term $\Delta\phi^{(k)}$ by:

$$J(\phi^{(k)}) \Delta\phi^{(k)}(x) = -R^{(k)}(x), \quad (A9)$$

Where $J(\phi^{(k)}) = \partial R / \partial \phi$ is the Jacobian matrix, constructed at each iteration numerically. The electrostatic potential for the next iteration is then updated as:

$$\phi^{(k+1)}(x) = \phi^{(k)}(x) + \alpha \cdot \Delta\phi^{(k)}(x), \quad (A10)$$

TABLE III. Key parameters used in the S-P calculation.

Parameter	Description	Value	Refs.
E_{Av}	Valence band offset	114 meV	[22,46]
m_{Ge}^*	Hole effective mass in Ge	0.0728	[5]
t_{SiO_x}	SiO _x layer thickness	1.5 nm	[23]
t_{SiGe}	Si _{0.2} Ge _{0.8} barrier thickness	32 nm	[5]
t_{Ge}	Ge QW thickness	16 nm	[5]
Δx	Mesh size	0.05 nm	/
α	Damping coefficient	[0.0001, 0.8]	/

with α as a damping coefficient $0 < \alpha \leq 1$ to ensure numerical stability. Note that in Newton's method we did not explicitly solve Poisson's equation as we did in Schrödinger, instead the update value of electrostatic potential in each step of iteration is computed numerically.

The convergence of the calculation is handled by monitoring the maximum change of potential energy, *i.e.*, the valence band profile, after each update:

$$conv = \max |V^{(k)}(x) - V^{(k-1)}(x)|. \quad (A11)$$

The iteration continues until the criterion $conv < 10 \mu\text{eV}$ is satisfied.

While conventional S-P solvers focus on the band profile of semiconductor heterostructures, we extend this by including the dielectric layers to consider the impact of interface charges. Specifically speaking, the material used in calculation is the full AlO_x/SiO_x/Si_{0.2}Ge_{0.8}/Ge/Si_{0.2}Ge_{0.8} stack (Fig. 1(b)). When solving Schrödinger's equation, we only consider the QW stack of Si_{0.2}Ge_{0.8}/Ge/Si_{0.2}Ge_{0.8} to obtain hole wavefunctions; when solving Poisson's equation, the full stack is used, in which gate voltage V_g is set as a Dirichlet boundary condition from the left side and filled interface traps p_{it} is treated as fixed positive charge within the SiO_x layer. Solving the S-P equation iteratively yields the self-consistent profile of valance band $E_v(x)$ and hole space distribution $p(x)$ under a given V_g and p_{it} . In order to transform the space charge density of holes (unit: C/m³) into sheet density consistent with experiments (unit: cm⁻² or m⁻²), we additionally calculate:

$$p_{2DHG,th} = \frac{1}{e} \int_{x_1}^{x_2} p(x) dx, \quad (A12)$$

where x_1 and x_2 are indices defining the region of germanium quantum well. This ultimately defines the output of S-P calculation as a single mapping explained in Eq. (1) of main text.

The material parameters used in the S-P solver are obtained from either literatures or linear interpolation

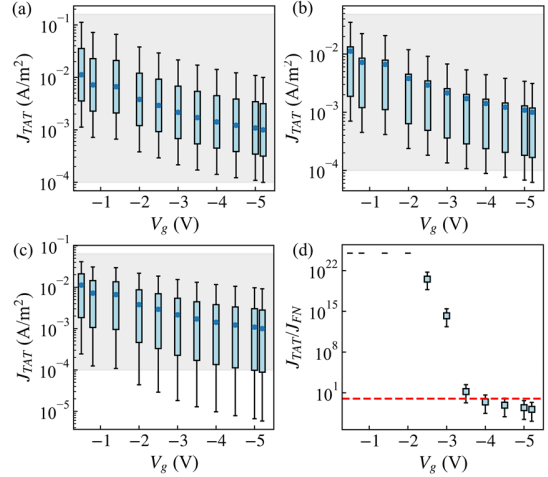


FIG. 6. Sensitivity test results of TAT current density in Ge/SiGe. J_{TAT} is evaluated under varied (a) trap density, (b) hole capture cross section and (c) trap energy respectively. Blue scatters indicate J_{TAT} under default parameter, boxes indicate J_{TAT} under varied trap parameters in TABLE I, grey shaded area indicates J_{TAT} order consistent with experiments. (d) Ratio of J_{TAT}/J_{FN} combining results from (a) to (c). Numerical explosion values with extremely small J_{FN} under small $|V_g|$ are capped and not shown. Red horizontal line indicates reference position where $J_{TAT} = J_{FN}$.

of SiGe alloy. Some of the key parameters are summarized in TABLE III.

APPENDIX B: SENSITIVITY OF TRAP-ASSISTED TUNNELING CURRENT DENSITY TO TRAP PARAMETERS

In the main text, trap-assisted tunneling (TAT) current density is calculated using a model that involves several microscopic parameters of dislocation-related traps in SiGe barrier, which are not directly available from our experiment. As a result, the calculated TAT current density J_{TAT} should be regarded as an order-of-magnitude estimate. The purpose of this section is to assess how sensitive the calculations are to the trap parameters and demonstrate that the two-regime picture suggested in the manuscript persists over a physically reasonable parameter range.

We focus on three trap parameters that strongly influence the calculation: the dislocation-related trap density N_{trap} , capture cross section for holes σ and the mean trap energy μ_{trap} used in Gaussian energy

distribution. For each of the three parameters, we select a range consistent with reported values for dislocation-related traps in Ge or Ge-based platforms. The chosen values are summarized in TABLE I. For each parameter, we set a baseline value and a corresponding test range. While keeping the other two parameters at their baseline values, we recompute $J_{TAT}(V_g)$ using the same S-P valence band profile in the main text, and sweep the parameter under test over the specified range. The results for J_{TAT} are shown in Fig. 7(a), (b) and (c) for variations of trap density, capture cross section and trap energy respectively. Fig. 4(e) in the main text combines all these results. We find that the values of J_{TAT} obtained in parameter tests mostly fall into this range, indicating that TAT provides a possible leakage path with the correct order of magnitude to account for the interface-state filling under small $|V_g|$ observed in the experiment.

In addition, we compare $J_{TAT}(V_g)$ and the Fowler-Nordheim tunneling current density $J_{FN}(V_g)$ for

different trap parameters by plotting the ratio of J_{TAT}/J_{FN} in Fig. 7(d). We find that while the absolute J_{TAT}/J_{FN} values depend on trap parameters, the qualitative two-regime picture persists. For all parameter sets in TABLE I, TAT dominates at small and moderate gate bias, whereas F-N tunneling dominates at large negative gate bias, and the crossover between two mechanisms occurs consistently at $V_g \approx -4.0$ V. This confirms that the mechanism discussed in Sec. V and Fig. 4(f) is not from an arbitrary choice of trap parameters, but from values supported by relevant literatures with physical robustness.

- [1] H. Watzinger, J. Kukučka, L. Vukušić, F. Gao, T. Wang, F. Schäffler, J.-J. Zhang, and G. Katsaros, A germanium hole spin qubit, *Nat. Commun.* **9**, 3902 (2018).
- [2] A. Sammak et al., Shallow and Undoped Germanium Quantum Wells: A Playground for Spin and Hybrid Quantum Technology, *Adv. Funct. Mater.* **29**, 1807613 (2019).
- [3] G. Scappucci, C. Kloeffel, F. A. Zwanenburg, D. Loss, M. Myronov, J.-J. Zhang, S. De Franceschi, G. Katsaros, and M. Veldhorst, The germanium quantum information route, *Nat. Rev. Mater.* **6**, 926 (2020).
- [4] N. W. Hendrickx, D. P. Franke, A. Sammak, G. Scappucci, and M. Veldhorst, Fast two-qubit logic with holes in germanium, *Nature* **577**, 487 (2020).
- [5] Z. Kong et al., Undoped Strained Ge Quantum Well with Ultrahigh Mobility of Two Million, *ACS Appl. Mater. Interfaces* **15**, 28799 (2023).
- [6] Y.-X. Li, Z. Kong, S. Hou, G. Wang, and S. Huang, Quantum transport quality of a processed undoped Ge/SiGe heterostructure, *Phys. Rev. B* **108**, 045303 (2023).
- [7] N. W. Hendrickx, W. I. L. Lawrie, M. Russ, F. van Riggelen, S. L. de Snoo, R. N. Schouten, A. Sammak, G. Scappucci, and M. Veldhorst, A four-qubit germanium quantum processor, *Nature* **591**, 580 (2021).
- [8] T.-K. Hsiao et al., Exciton Transport in a Germanium Quantum Dot Ladder, *Phys. Rev. X* **14**, 011048 (2024).
- [9] F. Borsoi, N. W. Hendrickx, V. John, M. Meyer, S. Motz, F. van Riggelen, A. Sammak, S. L. de Snoo, G. Scappucci, and M. Veldhorst, Shared control of a 16 semiconductor quantum dot crossbar array, *Nat. Nanotechnol.* **19**, 21 (2024).
- [10] V. John et al., Robust and localised control of a 10-spin qubit array in germanium, *Nat. Commun.* **16**, 10560 (2025).
- [11] C.-A. Wang et al., Operating semiconductor quantum processors with hopping spins, *Science* **385**, 447 (2024).
- [12] Y.-C. Zhou et al., High-fidelity geometric quantum gates exceeding 99.9% in germanium quantum dots, *Nat. Commun.* **16**, 7953 (2025).
- [13] V. P. Michal, J. C. Abadillo-Uriel, S. Zihlmann, R. Maurand, Y.-M. Niquet, and M. Filippone, Tunable hole spin-photon interaction based on g-matrix modulation, *Phys. Rev. B* **107**, L041303 (2023).
- [14] Y. Kang et al., Coupling of a hole double quantum dot in planar germanium to a microwave cavity, *Phys. Rev. Appl.* **22**, 024054 (2024).
- [15] F. De Palma, F. Oppiger, W. Jang, S. Bosco, M. Janík, S. Calcaterra, G. Katsaros, G. Isella, D. Loss, and P. Scarlino, Strong hole-photon coupling in planar Ge for probing charge degree and strongly correlated states, *Nat. Commun.* **15**, 10177 (2024).
- [16] M. Janík et al., Strong charge-photon coupling in planar germanium enabled by granular

aluminium superconductors, *Nat. Commun.* **16**, 2103 (2025).

[17] F. van Riggelen-Doelman, C.-A. Wang, S. L. de Snoo, W. I. L. Lawrie, N. W. Hendrickx, M. Rimbach-Russ, A. Sammak, G. Scappucci, C. Déprez, and M. Veldhorst, Coherent spin qubit shuttling through germanium quantum dots, *Nat. Commun.* **15**, 5716 (2024).

[18] N. H. Thoan, K. Keunen, V. V. Afanasev, and A. Stesmans, Interface state energy distribution and Pb defects at Si(110)/SiO₂ interfaces: Comparison to (111) and (100) silicon orientations, *J. Appl. Phys.* **109**, 013710 (2011).

[19] P. C. Spruijtenburg, S. V. Amitonov, W. G. van der Wiel, and F. A. Zwanenburg, A fabrication guide for planar silicon quantum dot heterostructures, *Nanotechnology* **29**, 143001 (2018).

[20] T. A. Hutchins-Delgado, A. J. Miller, R. Scott, P. Lu, D. R. Luhman, and T.-M. Lu, Characterization of Shallow, Undoped Ge/SiGe Quantum Wells Commercially Grown on 8-in. (100) Si Wafers, *ACS Appl. Electron. Mater.* **4**, 4482 (2022).

[21] Y.-H. Su, Y. Chuang, C.-Y. Liu, J.-Y. Li, and T.-M. Lu, Effects of surface tunneling of two-dimensional hole gases in undoped Ge/GeSi heterostructures, *Phys. Rev. Mater.* **1**, 044601 (2017).

[22] L. Massai et al., Impact of interface traps on charge noise and low-density transport properties in Ge/SiGe heterostructures, *Commun. Mater.* **5**, 151 (2024).

[23] Z.-H. Li et al., Impact of surface passivation on the electrical stability of strained germanium devices, *Chin. Phys. B* **34**, 090305 (2025).

[24] D. Laroche, S.-H. Huang, E. Nielsen, Y. Chuang, J.-Y. Li, C. W. Liu, and T. M. Lu, Scattering mechanisms in shallow undoped Si/SiGe quantum wells, *AIP Adv.* **5**, 107106 (2015).

[25] Y.-X. Li, Z. Kong, S. Hou, G. Wang, and S. Huang, Quantum transport quality of a processed undoped Ge/SiGe heterostructure, *Phys. Rev. B* **108**, 045303 (2023).

[26] Z. Kong et al., *High Mobility SiGe/Ge 2DHG Heterostructure Quantum Wells for Semiconductor Hole Spin Qubits*, arXiv:2410.00768.

[27] N. Sangwan, E. Jutzi, C. Olsen, S. Vogel, A. Nigro, I. Zardo, and A. Hofmann, *Impact of Surface Treatments on the Transport Properties of Germanium 2DHGs*, arXiv:2411.03995.

[28] L. Ruggiero, A. Nigro, I. Zardo, and A. Hofmann, A Backgate for Enhanced Tunability of Holes in Planar Germanium, *Nano Lett.* **24**, 13263 (2024).

[29] Y. Zhang et al., Ultrashallow heavily constrained quantum wells: The cradle for fully electrically controlled and microwave coupled quantum bits, *Phys. Rev. Mater.* **8**, 046203 (2024).

[30] B. Martinez and Y.-M. Niquet, Variability of Electron and Hole Spin Qubits Due to Interface Roughness and Charge Traps, *Phys. Rev. Appl.* **17**, 024022 (2022).

[31] M. A. Wolfe et al., Control of threshold voltages in Si / Si 0.7 Ge 0.3 quantum devices via optical illumination, *Phys. Rev. Appl.* **22**, 034044 (2024).

[32] W. Ha et al., A flexible design platform for Si/SiGe exchange-only qubits with low disorder, *Nano Lett.* **22**, 1443 (2022).

[33] I.-H. Tan, G. L. Snider, L. D. Chang, and E. L. Hu, A self-consistent solution of Schrödinger–Poisson equations using a nonuniform mesh, *J. Appl. Phys.* **68**, 4071 (1990).

[34] J. H. Luscombe, A. M. Bouchard, and M. Luban, Electron confinement in quantum nanostructures: Self-consistent Poisson–Schrödinger theory, *Phys. Rev. B* **46**, 10262 (1992).

[35] A. Gehring, *Simulation of Tunneling in Semiconductor Devices*, 1975.

[36] J. M. Beebe, B. Kim, J. W. Gadzuk, C. Daniel Frisbie, and J. G. Kushmerick, Transition from Direct Tunneling to Field Emission in Metal–Molecule–Metal Junctions, *Phys. Rev. Lett.* **97**, 026801 (2006).

[37] R. H. Fowler and L. Nordheim, Electron emission in intense electric fields, *Proc. R. Soc. Lond. Ser. Contain. Pap. Math. Phys. Character* **119**, 173 (1997).

[38] V. I. Vdovin, M. G. Mil'vidskii, M. M. Rzaev, and F. Schäffler, Misfit Dislocations in SiGe/Si Heterostructures: Nucleation – Propagation – Multiplication, *Solid State Phenom.* **108–109**, 483 (2005).

[39] S. Marchionna, A. Virtuani, M. Acciarri, G. Isella, and H. von Kaenel, Defect imaging of SiGe strain relaxed buffers grown by LEPECVD, *Mater. Sci. Semicond. Process.* **9**, 802 (2006).

[40] L. E. A. Stehouwer, A. Tosato, D. Degli Esposti, D. Costa, M. Veldhorst, A. Sammak, and G. Scappucci, Germanium wafers for strained quantum wells with low disorder, *Appl. Phys. Lett.* **123**, (2023).

[41] M. V. Berry and K. E. Mount, Semiclassical approximations in wave mechanics, *Rep. Prog. Phys.* **35**, 315 (1972).

[42] S. Makram-Ebeid and M. Lannoo, Quantum model for phonon-assisted tunnel ionization of deep levels in a semiconductor, *Phys. Rev. B* **25**, 6406 (1982).

[43] M. Zhang, Z. Huo, Z. Yu, J. Liu, and M. Liu, Unification of three multiphonon trap-assisted tunneling mechanisms, *J. Appl. Phys.* **110**, 114108 (2011).

[44] S. Gupta, E. Simoen, H. Vrielinck, C. Merckling, B. Vincent, F. Gencarelli, R. Loo, and M. Heyns, Identification of Deep Levels Associated with Extended and Point Defects in GeSn Epitaxial Layers Using DLTs, *ECS Trans.* **53**, 251 (2013).

[45] H. Tetzner, W. Seifert, O. Skibitzki, Y. Yamamoto, M. Lisker, M. M. Mirza, I. A. Fischer, D. J. Paul, M. De Seta, and G. Capellini, Unintentional p-type conductivity in intrinsic Ge-rich SiGe/Ge heterostructures grown on Si(001), *Appl. Phys. Lett.* **122**, 243503 (2023).

[46] F. Schäffler, High-mobility Si and Ge structures, *Semicond. Sci. Technol.* **12**, 1515 (1997).

[47] V. I. Vdovin, M. G. Mil'vidskii, M. M. Rzaev, and F. Schäffler, Misfit Dislocations in SiGe/Si Heterostructures: Nucleation - Propagation - Multiplication, *Solid State Phenom.* **108–109**, 483 (2005).

[48] N. A. DiLello, D. K. Johnstone, and J. L. Hoyt, Characterization of dark current in Ge-on-Si photodiodes, *J. Appl. Phys.* **112**, 054506 (2012).

[49] C. G. Van De Walle and R. M. Martin, Theoretical calculations of heterojunction discontinuities in the Si/Ge system, *Phys. Rev. B* **34**, 5621 (1986).

[50] L. F. Peña, J. C. Koepke, J. H. Dycus, A. Mounce, A. D. Baczewski, N. T. Jacobson, and E. Bussmann, Modeling Si/SiGe quantum dot variability induced by interface disorder reconstructed from multiperspective microscopy, *Npj Quantum Inf.* **10**, 33 (2024).

[51] K. Lai, P. D. Ye, W. Pan, D. C. Tsui, S. A. Lyon, M. Mühlberger, and F. Schäffler, Modulation of the high mobility two-dimensional electrons in SiSiGe using atomic-layer-deposited gate dielectric, *Appl. Phys. Lett.* **87**, 142103 (2005).

[52] E. A. Fitzgerald, M. T. Currie, S. B. Samavedam, T. A. Langdo, G. Taraschi, V. Yang, C. W. Leitz, and M. T. Bulsara, Dislocations in Relaxed SiGe/Si Heterostructures, *Phys. Status Solidi A* **171**, 227 (1999).

[53] A. Sakai, K. Sugimoto, T. Yamamoto, M. Okada, H. Ikeda, Y. Yasuda, and S. Zaima, Reduction of threading dislocation density in SiGe layers on Si (001) using a two-step strain-relaxation procedure, *Appl. Phys. Lett.* **79**, 3398 (2001).

[54] A. D. Capewell, T. J. Grasby, T. E. Whall, and E. H. C. Parker, Terrace grading of SiGe for high-quality virtual substrates, *Appl. Phys. Lett.* **81**, 4775 (2002).

[55] Yu. B. Bolkhovityanov, A. S. Deryabin, A. K. Gutakovskii, M. A. Revenko, and L. V. Sokolov, Strain relaxation of GeSi/Si(001) heterostructures grown by low-temperature molecular-beam epitaxy, *J. Appl. Phys.* **96**, 7665 (2004).

[56] P. N. Grillot, S. A. Ringel, E. A. Fitzgerald, G. P. Watson, and Y. H. Xie, Electron trapping kinetics at dislocations in relaxed Ge0.3Si0.7/Si heterostructures, *J. Appl. Phys.* **77**, 3248 (1995).

[57] R. People and J. C. Bean, Calculation of critical layer thickness versus lattice mismatch for $\text{Ge}_{x}\text{Si}_{1-x}/\text{Si}$ strained-layer heterostructures, *Appl. Phys. Lett.* **47**, 322 (1985).

[58] J. C. Bean, Strained-Layer Epitaxy of Germanium-Silicon Alloys, *Science* **230**, 127 (1985).

[59] Md. M. Alam, Y. Wagatsuma, K. Okada, Y. Hoshi, M. Yamada, K. Hamaya, and K. Sawano, Critical thickness of strained $\text{Si}_{1-x}\text{Ge}_x$ on Ge(111) and Ge-on-Si(111), *Appl. Phys. Express* **12**, 081005 (2019).

[60] D. Costa, P. D. Vecchio, K. Hudson, L. E. A. Stehouwer, A. Tosato, D. D. Esposti, M. Lodari, S. Bosco, and G. Scappucci, *Buried Unstrained Germanium Channels: A Lattice-Matched Platform for Quantum Technology*, arXiv:2506.04724.

[61] L. Mauro, M. J. Rodríguez, E. A. Rodríguez-Mena, and Y.-M. Niquet, Hole spin qubits in unstrained Germanium layers, *Npj Quantum Inf.* **11**, 167 (2025).

[62] A. Secchi, G. Forghieri, P. Bordone, D. Loss, S. Bosco, and F. Troiani, *Hole-Spin Qubits in Germanium beyond the Single-Particle Regime*, arXiv:2505.02449.

[63] E. Valvo, M. Jakob, P. D. Vecchio, M. Rimbach-Russ, and S. Bosco, *Electrically Tuneable Variability in Germanium Hole Spin Qubits*, arXiv:2512.12702.

[64] O. Skibitzki et al., Reduction of threading dislocation density beyond the saturation limit by optimized reverse grading, *Phys. Rev. Mater.* **4**, 103403 (2020).

[65] K. Sardashti et al., Sulfur passivation for the formation of Si-terminated $\text{Al}_2\text{O}_3/\text{SiGe}(0\ 0\ 1)$ interfaces, *Appl. Surf. Sci.* **366**, 455 (2016).

[66] F. Aguirre, S. Pazos, F. R. M. Palumbo, S. Fadida, R. Winter, and M. Eizenberg, Effect of forming gas annealing on the degradation properties of Ge-based MOS stacks, *J. Appl. Phys.* **123**, 134103 (2018).

- [67] W. J. H. (Willem-Jan) Berghuis, J. Melskens, B. Macco, R. J. Theeuwes, L. E. Black, M. A. Verheijen, and W. M. M. (Erwin) Kessels, Excellent surface passivation of germanium by a-Si:H/Al₂O₃ stacks, *J. Appl. Phys.* **130**, 135303 (2021).
- [68] L. Zhou, J. Xiang, X. Wang, and W. Wang, Investigation on the passivation, band alignment, gate charge, and mobility degradation of the Ge MOSFET with a GeO_x/Al₂O₃ gate stack by ozone oxidation, *J. Semicond.* **43**, 013101 (2022).